Linear Versus Nonlinear Signal Transmission in Neuron Models With Adaptation Currents or Dynamic Thresholds

Jan Benda, Leonard Maler and André Longtin

You might find this additional info useful...

This article cites 49 articles, 17 of which you can access for free at:
http://jn.physiology.org/content/104/5/2806.full#ref-list-1

This article has been cited by 3 other HighWire-hosted articles:
http://jn.physiology.org/content/104/5/2806#cited-by

Updated information and services including high resolution figures, can be found at:
http://jn.physiology.org/content/104/5/2806.full

Additional material and information about *Journal of Neurophysiology* can be found at:
http://www.the-aps.org/publications/jn

This information is current as of February 20, 2013.

Linear Versus Nonlinear Signal Transmission in Neuron Models With Adaptation Currents or Dynamic Thresholds

Jan Benda,[1] Leonard Maler,[2] and André Longtin[2,3]

[1]*Division of Neurobiology, Department Biology II, Ludwig-Maximilians-Universität München, Planegg-Martinsried, Germany; and* [2]*Department of Cellular and Molecular Medicine and* [3]*Department of Physics, University of Ottawa, Ottawa, Canada*

Benda J, Maler L, Longtin A. Linear versus nonlinear signal transmission in neuron models with adaptation currents or dynamic thresholds. *J Neurophysiol* 104: 2806–2820, 2010; doi:10.1152/jn.00240.2010. Spike-frequency adaptation is a prominent aspect of neuronal dynamics that shapes a neuron's signal processing properties on timescales ranging from about 10 ms to >1 s. For integrate-and-fire model neurons spike-frequency adaptation is incorporated either as an adaptation current or as a dynamic firing threshold. Whether a physiologically observed adaptation mechanism should be modeled as an adaptation current or a dynamic threshold, however, is not known. Here we show that a dynamic threshold has a divisive effect on the onset *f–I* curve (the initial maximal firing rate following a step increase in an input current) measured at increasing mean threshold levels, i.e., adaptation states. In contrast, an adaptation current subtractively shifts this *f–I* curve to higher inputs without affecting its slope. As a consequence, an adaptation current acts essentially linearly, resulting in a high-pass filter component of the neuron's transfer function for current stimuli. With a dynamic threshold, however, the transfer function strongly depends on the input range because of the multiplicative effect on the *f–I* curves. Simulations of conductance-based spiking models with adaptation currents, such as afterhyperpolarization (AHP)-type, M-type, and sodium-activated potassium currents, do not show the divisive effects of a dynamic threshold, but agree with the properties of integrate-and-fire neurons with adaptation current. Notably, the effects of slow inactivation of sodium currents cannot be reproduced by either model. Our results suggest that, when lateral shifts of the onset *f–I* curve are seen in response to adapting inputs, adaptation should be modeled with adaptation currents and not with a dynamic threshold. In contrast, when the slope of onset *f–I* curves depends on the adaptation state, then adaptation should be modeled with a dynamic threshold. Further, the observation of divisively altered onset *f–I* curves in adapted neurons with notable variability of their spike threshold could hint to yet known biophysical mechanisms directly affecting the threshold.

INTRODUCTION

Adaptation is a common property of many neurons and plays an important role in neuronal information processing. In particular, spike-frequency adaptation caused by a variety of adaptation currents explains, for example, forward masking of weaker stimuli (Sobel and Tank 1994), enhancement of the response to fast stimulus components (Benda et al. 2005), or selective responses to looming stimuli (Peron and Gabbiani 2009). Incorporating an adaptation mechanism in neuron models for simulations of experimentally observed responses to dynamical inputs is therefore necessary for capturing the full functional repertoire of neurons.

The most prominent ionic currents inducing spike-frequency adaptation are voltage- or calcium-gated potassium currents (Brown and Adams 1980; Madison and Nicoll 1984; Sah 1996). Similarly, sodium-activated potassium currents also cause spike-frequency adaptation on much longer timescales (many seconds; Wang et al. 2003). All these inhibitory potassium currents are activated directly or indirectly during action potentials. In contrast, slow inactivation of the sodium current slowly reduces the availability of sodium channels that can be activated and thus directly reduces the neuron's excitability (Fleidervish et al. 1996). Whether there is a unique and generic way how to extend neuron models, especially integrate-and-fire models, is a priori not clear, given this diversity of possible mechanisms for spike-frequency adaptation. Herein we investigate, in particular, the difference between adaptation mechanisms acting as ionic currents and mechanisms directly influencing the neuron's firing threshold.

Integrate-and-fire models have a long history as the most simple models of spiking activity (Lapicque 1907; Stein 1965). In these models a stimulus and/or noise drive the membrane voltage toward a firing threshold. Once the threshold is crossed, a spike is emitted and the voltage is reset. Early extensions of the integrate-and-fire model introduced a dependence of the firing threshold on the time since the last spike. With such models experimentally observed variability of interspike intervals (ISIs) (Geisler and Goldberg 1966; Holden 1976; Wilbur and Rinzel 1983) or effects of AHPs (Tuckwell 1978) have been phenomenologically reproduced. However, the hard reset of both the voltage and the threshold variable makes cumulative phenomena like spike-frequency adaptation, which evolve over many ISIs, impossible (Fohlmeister 1979; Lindner and Longtin 2005).

By cumulatively adding an exponentially decaying AHP to the membrane voltage after each spike, Geisler and Goldberg (1966) successfully modeled negative ISI correlations that are also commonly observed in neural activity (Farkhooi et al. 2009). For simulating spike-frequency adaptation in auditory nerve fibers Bibikov and Ivanitskíí (1985) used a dynamic threshold that was incremented by each spike event and that then decayed back. This concept was reintroduced as a possible model reproducing spike-frequency adaptation and the associated negative correlations of successive ISIs (Chacron et al. 2000; Liu and Wang 2001). The latter was shown to increase the transinformation between a stimulus and the evoked spike train by reducing low-frequency noise (Chacron et al. 2001, 2005, 2007; Lindner et al. 2005).

An alternative way for generating spike-frequency adaptation with integrate-and-fire models is to subtract a feedback variable from the stimulus (Fohlmeister 1979), i.e., add an adaptation current directly to the membrane equation (Gigante et al. 2007; Treves 1993). Recently, various types of integrate-and-fire models with adaptation current have been shown to reproduce spiking activity of cortical pyramidal cells (Jolivet et al. 2008; Rauch et al. 2003).

Liu and Wang (2001) compared the two methods—adaptation current and dynamic threshold—for generating spike-frequency adaptation in integrate-and-fire neurons. They found subtle differences regarding the dependence of the adaptation time constant on input current and of the ISI variability on time after stimulus onset. Here, however, we demonstrate that an adaptation current has a qualitatively different effect on the neuron's transfer function than that of a dynamic threshold. Our results can therefore be used to distinguish adaptation mechanisms primarily acting as currents or affecting the firing threshold.

First, by the example of the leaky integrate-and-fire neuron we show that adaptation modeled by a dynamic threshold has a nonlinear effect on the neuron's transfer function, whereas an adaptation current acts linearly. By contrasting these results with simulations on a number of conductance-based models with various adaptation currents, we conclude that only an adaptation current added to an integrate-and-fire neuron can reproduce the properties of the more realistic conductance-based model. For the perfect integrate-and-fire neuron we provide analytical expressions for onset spike frequency versus input current (f–I) curves, demonstrating the divisive effect of the dynamic threshold versus the subtractive effect of adaptation currents. Averaging theory allows us to immediately assess the impact of a dynamic threshold, given an analytical expression for the firing rate of an integrate-and-fire neuron without any adaptation process. Finally, we discuss the two adaptation mechanisms in both the quadratic (Ermentrout and Kopell 1986) and the exponential integrate-and-fire neuron (Fourcaud-Trocmé et al. 2003).

METHODS

All integrate-and-fire models as well as the conductance-based models were integrated using the Euler-forward method, with time steps of $\Delta t = 0.005$ ms or sometimes $\Delta t = 0.01$ ms. Only for computing the ISI correlations was a white Gaussian noise $\eta(t)$ of intensity D [i.e., with correlation function $\langle \eta(t)\eta(t') \rangle = 2D\delta(t - t')$] added to the constant input current. For this, the term $\sqrt{2D/\Delta t}\, N(0, 1)$ was added to the right-hand side of the current balance equation before applying the standard Euler integration technique, where $N(0, 1)$ is a normally distributed random number that was drawn in each time step. In all other simulations the models were deterministic.

If not stated otherwise, the standard parameters for the integrate-and-fire models were membrane time constant $\tau_V = 10$ ms, firing threshold $V_{th} = 10$ mV, reset potential $V_r = 0$ mV, input resistance $R = 1$ MΩ, adaptation time constant $\tau_A = 100$ ms, adaptation strength $\Delta A = 2$ nA for adaptation currents, and $\Delta A = 2$ mV for dynamic thresholds. The conductance-based models are specified in the APPENDIX.

Spike frequency as a function of time was obtained by assigning for each time t (in 1-ms increments) the inverse ISI that contains this time t. Consequently, the onset spike frequency f_0 is the inverse of the first ISI following the onset of a step input.

To compute the transfer function we stimulated the neuron models using low-pass filtered white noise. This noise was generated by first initializing in Fourier space both the real and the imaginary parts of all frequencies up to the cutoff frequency f_c, with independent random numbers drawn from a Gaussian distribution of zero mean and unit SD. After fast Fourier back-transformation and division by $\sqrt{4\Delta t N f_c}$, where N is the number of data points (a power of two), this results in a smooth curve sampled every $\Delta t = 1$ ms.

The stimulated spike train in response to the low-pass filtered white noise stimulus $I(t)$ was converted into a time series $r(t)$ of zeros and ones with a bin width of 1 ms, where the ones represent the occurrences of spikes. The gain of the transfer function was then computed as

$$g(\omega) = \left| \frac{\langle \tilde{r}\tilde{I}* \rangle}{\langle \tilde{I}\tilde{I}* \rangle} \right| \tag{1}$$

where $\tilde{r}$ and $\tilde{I}$ are mean-subtracted and Fourier-transformed chunks of the spike train and input, respectively. $\langle \tilde{I}\tilde{I}* \rangle$ is the power spectrum of the input current and $\langle \tilde{r}\tilde{I}* \rangle$ is the cross-spectrum between input current and output spike train. The angled brackets $\langle \cdot \rangle$ denote averaging over chunks of 2^{20} data points ($= 5.24288$ s @ $\Delta t = 0.05$ ms) that were windowed using the Bartlett window function and overlapped by half the size of a window. For the analysis, the transient initial adaptation during the first second was discarded from the 10,000 s long simulations to ensure steady state as required for computing the transfer function.

The serial correlation between successive ISIs was computed from 50,000 or 100,000 simulated ISIs T_i by means of

$$C_{ISI} = \frac{\langle (T_i - \langle T_i \rangle)(T_{i+1} - \langle T_i \rangle) \rangle}{\langle (T_i - \langle T_i \rangle)^2 \rangle} \tag{2}$$

Here, the angled brackets denote averaging over all ISIs; $\langle T_i \rangle$ is the mean ISI.

RESULTS

Before we present our results, let us first introduce the leaky integrate-and-fire (LIF) neuron and its two adapting variants with adaptation current or dynamic threshold.

Leaky integrate-and-fire neuron

The LIF models a neuron in the subthreshold regime as a linear membrane with time constant τ_V and input resistance R. The dynamics of the membrane potential V in response to the injected current $I(t)$ that is a predefined function of time t is given by

$$\tau_V \frac{dV}{dt} = -V + R \cdot I(t) \tag{3}$$

Whenever V crosses the threshold V_{th}, a spike is emitted and V is reset to the reset potential V_r. Note that throughout this study we set the resting potential of all integrate-and-fire neurons to zero.

An adaptation current $I_A = \bar{g}_A a(V - E_A)$, with maximum conductance $\bar{g}_A$, gating variable a, and reversal potential E_a, acts subtractively on the input I

$$\tau_V \frac{dV}{dt} = -V + R \cdot \left[I(t) - \bar{g}_A a(V - E_A) \right] \tag{4}$$

$$\tau_A \frac{da}{dt} = a_\infty(V) - a \tag{5}$$

The steady-state activation function $a_\infty(V)$ of the adaptation current is a sigmoidal function that is zero for low mem-

brane potentials and increases to one at potentials ideally well above the spiking threshold. Thus between spikes $a_\infty(V)$ is close to zero and therefore a decays back to zero with the adaptation time constant τ_A. During each spike, which is not explicitly modeled in the integrate-and-fire neurons, $a_\infty(V)$ takes on values close to one and a is therefore incremented, at each spike, by approximately a fixed amount Δa.

Approximating the driving force $V - E_A$ by a constant c and introducing a rescaled adaptation variable $A = a\bar{g}_A c$ one gets

$$\tau_V \frac{dV}{dt} = -V + R \cdot [I(t) - A] \tag{6}$$

$$\tau_A \frac{dA}{dt} = -A \tag{7}$$

On each threshold crossing the membrane potential is again reset to V_r and, in addition, A is incremented by $\Delta A = \Delta a\bar{g}_A c$ (Benda and Herz 2003). This is the leaky integrate-and-fire neuron with adaptation current (LIFAC; Liu and Wang 2001). Examples of the dynamics of the LIFAC and the resulting spike-frequency adaptation are shown in Fig. 1, A and C.

Alternatively to the adaptation current, a dynamic threshold also results in spike-frequency adaptation (Chacron et al. 2000; Liu and Wang 2001). The equation for the membrane voltage remains exactly that of the original LIF (*Eq. 3*), but the voltage threshold—now denoted by A—gets its own dynamics with the adaptation time constant τ_A

$$\tau_V \frac{dV}{dt} = -V + R \cdot I(t) \tag{8}$$

$$\tau_A \frac{dA}{dt} = -A + V_{th} \tag{9}$$

Whenever V crosses the dynamic threshold A, V is reset to V_r and A is incremented by ΔA as for the LIFAC. Between the spikes, A decays back to the minimum threshold V_{th}. This is the

leaky integrate-and-fire neuron with dynamic threshold (LIFDT; for an example see Fig. 1, *B* and *D*).

Distinct firing properties resulting from either adaptation currents or dynamic thresholds

Let us first introduce our basic findings on the example of the leaky integrate-and-fire neuron (LIFAC and LIFDT).

Adapted f–I curves. The input–output relation of a nonadapting neuron can be well captured by its *f–I* curve that relates the spike frequency *f* to the input current *I*. However, because of adaptation processes a description of the neuron's input–output relation by a single *f–I* curve is no longer sufficient. Depending on the current value of the adaptation variable *A*, different *f–I* curves describe the onset response of the neuron to changes in the input: the adapted *f–I* curves $f_0(I, A)$. A special case is the onset *f–I* curve $f_0(I)$ for the response of the unadapted neuron ($A = 0$). The subscript 0 used for the onset and adapted *f–I* curves refers to the onset response measured right after the onset of the test stimulus *I*. In addition, there is the steady-state *f–I* curve $f_\infty(I)$ describing the maximally adapted spike frequency for a given fixed input *I*. The steady-state response is measured a sufficiently long time after the constant test stimulus *I* was switched on ($t \to \infty$, as indicated by the subscript). We do not consider other *f–I* curves that are measured at intermediate times after stimulus onset, since the onset and the steady-state *f–I* curves are sufficient for a complete description of the adaptation dynamics (Benda and Herz 2003).

Such adapted onset *f–I* curves can be measured by first setting the input current $I(t)$ to a value I_0 for a time much longer than the adaptation time constant. At the end of this stimulus the neuron is completely adapted, the neuron fires along with its steady-state spike-frequency $f_\infty(I_0)$, and the adaptation variable has assumed a certain mean value $\langle A \rangle$ that solely depends on the value of I_0, i.e., $\langle A \rangle = \langle A \rangle(I_0)$. Then the input current $I(t)$ is stepped to a test value *I* and the resulting onset response, i.e., the maximum (in the case $I > I_0$) or minimum ($I < I_0$) spike
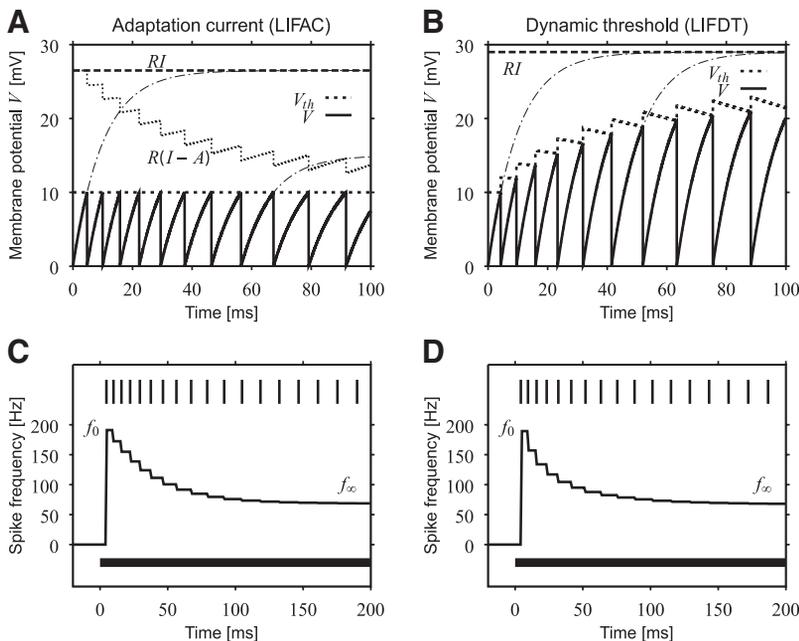

FIG. 1. Spike-frequency adaptation modeled as an adaptation current or dynamic threshold. *A*: the time course of the membrane potential (solid line) of the leaky integrate-and-fire neuron with adaptation current (LIFAC) in response to the onset of a constant current $I = 26.5$ nA (long dashed line) at time $t = 0$ ($I = 0$ for $t < 0$). The voltage threshold is fixed at $V_{th} = 10$ mV (short dashed line) but the steady-state potential $R(I - A)$ (dotted line) is reduced by the increasing adaptation current. The approach of the membrane potential is therefore slowed down as indicated by the dash-dotted lines showing the evolution of the membrane potential without voltage threshold. *B*: with a dynamic threshold the steady-state potential stays constant at RI (long dashed line), but the threshold is increased by each spike and therefore the membrane potential needs more time until it reaches the threshold. Input current was $I = 29$ nA to evoke the same onset response of about 190 Hz as in the example of the LIFAC. *C* and *D*: both mechanisms result in similar adapting spike-frequency responses. The initially high spike-frequency response (onset spike frequency f_0, which is computed as the inverse of first interspike interval [ISI]) to the onset of the constant stimulus (black bar) gradually decays down to a lower steady-state spike frequency f_∞. Spike frequency at time *t* is defined as the inverse of the ISI that contains *t*. The corresponding spike trains are shown at the *top* (vertical strokes). The parameter values used for both LIF models were $\tau_V = 10$ ms, $V_{th} = 10$ mV, $V_r = 0$ mV, $R = 1$ MΩ, $\tau_A = 100$ ms, $\Delta A = 2$ nA for LIFAC and $\Delta A = 2$ mV for leaky integrate-and-fire neuron with dynamic threshold (LIFDT).

frequency right after the onset of I, is then a point of the adapted f–I curve $f_0(I, A)$. Here $\langle A \rangle(I_0)$ is replaced by A for simplicity, to indicate that this f–I curve $f_0(I, A)$ is the onset spike frequency evoked by I, given a certain state of adaptation A, independent of the specific history of the stimulus and the adaptation dynamics. This also implies that we neglect the minimal changes of the adaptation variable already induced by the first spike in response to the test stimulus and the dynamics during the following ISI (compare the small variations of A during a single ISI with the large change over the whole course of the stimulus in Fig. 1, A and B). The whole procedure, i.e., adapt to I_0 and then measure onset response to I, is repeated for a range of test currents I, to sample a whole adapted f–I curve $f_0(I, A)$.

The concept of the adapted f–I curves that depend on the current level of adaptation facilitates an intuitive understanding of the neuron's signal transmission properties. Consider an input containing slow components (period far lower than the time constant of the adaptation dynamics) as well as much faster components (faster than the adaptation dynamics). The level of adaptation will follow the slow input and thus the adapted f–I curve will change accordingly. In contrast, adaptation cannot follow the fast stimulus and therefore a fast stimulus cannot change the adapted f–I curve. Note that the instantaneous increase of the adaptation variable on a spike does not significantly change the adapted f–I curve. As a consequence, at the peak or trough of the slow input the adapted f–I curves differ because of the different adaptation levels and so the response to the faster input will be different depending on where it occurs with respect to the phase of the slower signal components.

Adaptation currents have been shown to shift the adapted f–I curves horizontally to higher inputs (Benda and Herz 2003) and to linearize the steady-state f–I curve compared with the onset f–I curve (Ermentrout 1998).

The f–I curves of the LIFAC indeed follow these expectations (Fig. 2A). For spike frequencies above the steady-state f–I curve the three adapted f–I curves shown (open triangles) exactly match the onset f–I curve (open circles) appropriately shifted to the right (solid lines). Below the steady-state f–I curve the adapted f–I curves are overestimated because the initial low spike-frequency response (i.e., long ISI) is prema-

turely terminated by a spike generated when the adaptation level has substantially recovered, as described in Benda and Herz (2003). Also, the steady-state f–I curve has a reduced slope and is fairly linear over the whole range of input currents and more linear than the onset f–I curve.

In contrast, the adapted f–I curves of the LIFDT show a prominent reduction in their slope in addition to a small shift (Fig. 2B). Further, the steady-state f–I curve of the LIFDT is more curved than that of the LIFAC. Thus it is not linearized compared with the onset f–I curve in contrast to the LIFAC model.

Therefore a comparison of the effects of preadaptation on the f–I curves can indicate whether an adaptation current (simple shift, no change of slope) or a dynamic threshold (slope change) should be used to model physiological data.

Transfer functions. Stimulus components that are faster than the adaptation process are transmitted via the adapted f–I curve, since adaptation is too slow to follow such a stimulus and thus the adaptation level stays approximately fixed. Stimulus components that are slower than the adaptation dynamics are transmitted by the steady-state f–I curve, since there is enough time for the adaptation mechanisms to fully adapt. Since generally the slope (gain) of the steady-state f–I curve is smaller than that of the onset f–I curve, the transfer function between the stimulus and the resulting spike frequency acts as a high-pass filter with a cutoff frequency at $(2\pi s\tau_A)^{-1}$, where s is the slope of the steady-state f–I curve divided by that of the onset f–I curve (Benda and Hennig 2008; Benda and Herz 2003; Benda et al. 2005).

For an illustration of this effect, we computed transfer functions by stimulating the models with input currents $I(t) = I_0 + \sigma\eta(t)$, where $I_0 = \langle I \rangle$ is the mean stimulus, η is a Gaussian white noise with zero mean, and unit SD that was low-pass filtered with a cutoff frequency of 16 Hz (see METHODS). The SD σ of the noise was set to the small value of 2 nA to minimize effects introduced by the nonlinear shapes of the f–I curves. From the resulting spike response we then computed the gain of the transfer function (see METHODS).

Both adaptation current and dynamic threshold indeed produce a high-pass filter component to the neuron's transfer function (Fig. 3). In the LIFAC, however, the gain function is almost independent of the stimulus mean (Fig. 3A), whereas in
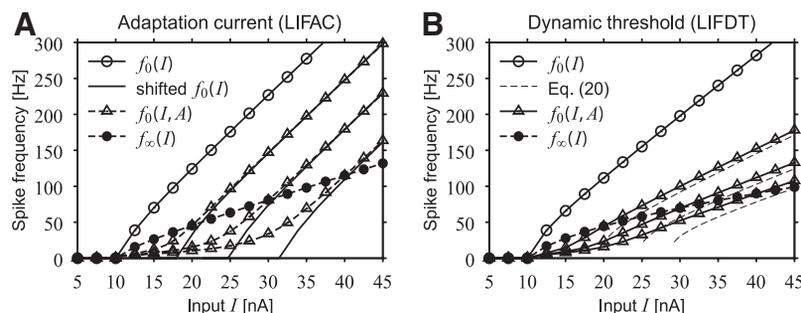

FIG. 2. Adaptation current has a subtractive, dynamic threshold a divisive effect on adapted onset spike frequency vs. input current (f–I) curves of leaky integrate-and-fire (LIF) models. Measuring the onset f_0 and the steady-state spike frequency f_∞ (see Fig. 1C) as a function of the input current I results in the onset $f_0(I)$ (open circles) and the steady-state f–I curve $f_\infty(I)$ (filled circles), respectively. Preadapting the neuron to various input currents $I(t < 0) = I_0$ (here $I_0 = $ 20, 30, 40 nA for both models) and thus corresponding states of adaptation A, and then measuring again the onset response to test currents I ($t > 0) = I$ (abscissa) results in adapted f–I curves $f_0(I, A)$ (open triangles) for these states of adaptation A. A: the onset and adapted f–I curves of the LIFAC for different levels of the adaptation current [$A(I_0) = 10, 17, 24$ nA]. The adapted f–I curves (open triangles) clearly match the onset f–I curve (open circles) shifted to the right such that it crosses each of the adapted f–I curves at a spike frequency of 200 Hz ["shifted $f_0(I)$", solid line]. B: adapted f–I curves of the LIFDT for different threshold values [$A(I_0) = 20, 25, 29$ mV]. Clearly, the adapting threshold has a divisive effect on the adapted f–I curves. The dashed lines are the predictions for the adapted f–I curves from the averaging theory (Eq. 20). Same parameter values as in Fig. 1.
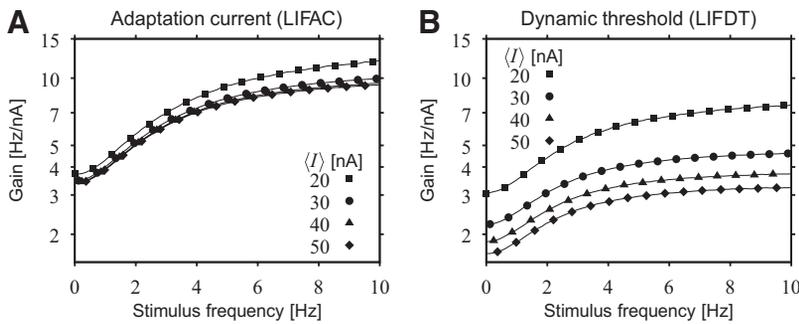
FIG. 3. Transfer functions of the leaky integrate-and-fire (LIF) models. The gain was computed using low-pass filtered (0–16 Hz) Gaussian white noise current stimuli with SD 2 nA and 4 different mean values $\langle I \rangle$ as indicated. *A*: for the LIFAC the gain functions for stimuli with different means are similar. *B*: in the LIFDT the overall gain is strongly reduced for higher mean values of the stimulus. Also, the difference in gain between high-frequency stimuli (>6 Hz) and low-frequency stimuli (<0.5 Hz) decreases for increasing $\langle I \rangle$ (nonlinear compression; note the logarithmic axis for the gain). Same parameter values as in Fig. 1.

the LIFDT the overall gain as well as the strength of the high-pass filter is reduced for higher mean inputs (Fig. 3*B*).

This can be completely understood by the *f–I* curves shown in Fig. 2. Since the steady-state *f–I* curve of the LIFAC is approximately linear, the gain at low stimulus frequencies is independent of the mean stimulus. The gain at high stimulus frequencies is also independent of the mean stimulus, since the adapted *f–I* curves are shifted versions of the onset *f–I* curves and thus all have the same gain. Only at low values of mean stimulus does the transfer function differ slightly from those obtained for stimuli with higher means because of the nonlinear shapes of the *f–I* curves close to input threshold.

With a dynamic threshold, however, the slope of the adapted *f–I* curves is reduced compared with the onset *f–I* curve and the slope of the steady-state *f–I* curve decreases for stimuli with higher mean values. Consequently, the gain of the transfer function for both fast and slow stimulus components is reduced for stimuli with higher mean intensities.

The effect of adding a constant offset or bias to a time-varying stimulus is a second powerful tool for deciding between adaptation currents versus a dynamic threshold. If the gain of the experimentally observed *f–I* curves is independent of the input bias, then an adapting current should be used for modeling. In contrast, when increasing the input bias diminishes the gain, then use of a dynamic threshold is indicated.

Negative ISI correlations. In addition to adapting the spike-frequency response, adaptation induces negative correlations between the duration of successive ISIs when the neuron is

driven with additive noise that may arise from ion channel stochasticity or random synaptic input (Chacron et al. 2000; Liu and Wang 2001; Wang 1998). After a short ISI the neuron is more strongly adapted and thus the following ISI is more likely to be longer and vice versa.

Both LIFAC and LIFDT generate similar negative ISI correlations in response to constant inputs with additive white noise (Fig. 4, *A–C*). The anticorrelation is largest for spike frequencies close to, but not identical to, one over the adaptation time constant. At lower firing rates the ISI correlations diminish, since adaptation decays away before the next spike. At high firing rates, on the other hand, the change in adaptation strength from one spike to the other is too small compared with the high-input currents. Note that with increasing noise strength the correlations diminish. The corresponding coefficients of variation (CVs) of the ISI distributions are also comparable between LIFAC and LIFDT and, for both models, the CVs are smaller than that of the LIF without adaptation mechanism (Fig. 4, *D–F*).

Conductance-based models behave like the LIFAC

The biophysical origins of spike-frequency adaptation are various types of ionic currents that are activated by spikes and slowly deactivate between spikes. Prominent examples are M-type currents (Brown and Adams 1980), AHP-type currents (Madison and Nicoll 1984; Sah 1996), sodium-activated potassium currents (Wang et al. 2003), or slow inactivation of the sodium current (Edman et al. 1987; Fleidervish et al. 1996).
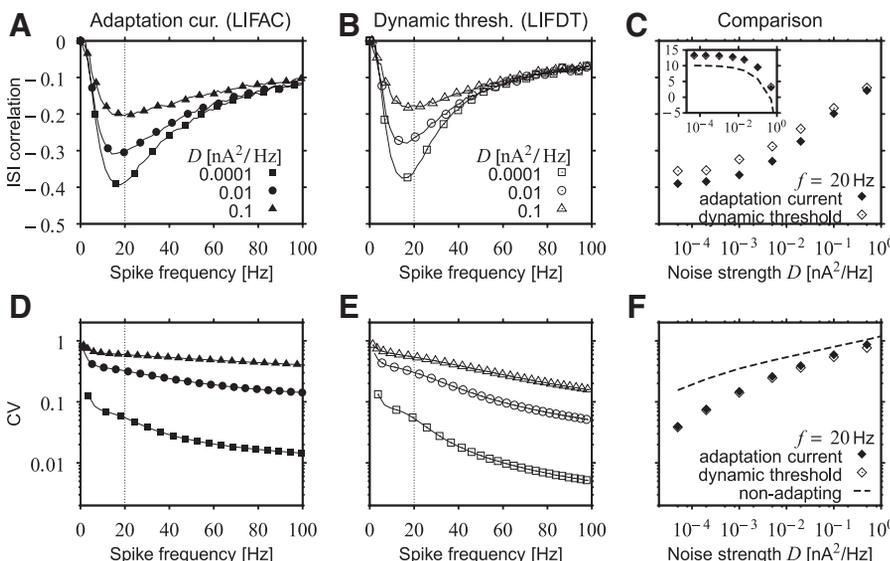

FIG. 4. Adaptation induces negative ISI correlations. Both leaky integrate-and-fire models with adaptation current (*A*, *D*) and dynamic threshold (*B*, *E*) show similar negative correlations between successive ISIs and coefficients of variation (CVs) of the ISIs in the steady-state when driven by constant currents with additive white Gaussian noise $\eta(t)$ of intensity D, i.e., $\langle \eta(t)\eta(t') \rangle = 2D\delta(t - t')$. *A* and *B*: the correlation between successive ISIs as a function of spike frequency and 3 different values of the noise strength D as indicated. Spike frequency was varied by means of the constant current. *C*: a comparison of the ISI correlations of the LIFAC and the LIFDT as a function of the noise strength D and an input current adjusted such that the resulting spike frequency was 20 Hz. The *inset* shows the required input current in nA, the dashed line the LIF without adaptation. *D* and *E*: the CV of the ISIs corresponding to the data shown in *A* and *B*. *F*: a comparison of the CVs. Additionally, the CV of the LIF without adaptation is plotted as the dashed line. Same parameter values as in Fig. 1.

M-type currents are slow potassium currents that are activated during action potentials. AHP-type currents and sodium-activated potassium currents are both potassium currents that are instantaneously gated by the intracellular concentration of calcium and sodium, respectively. The calcium/sodium concentration is increased by calcium/sodium influx during each spike and the slow adaptation dynamics is due to the slow removal of these ions from the cytoplasm. Whereas adaptation based on M-type and the AHP-type currents acts on roughly about 100 ms, adaptation caused by sodium-activated potassium currents is much slower (several seconds). Slow inactivation of the sodium current is a third gating variable of the spike-generating sodium current that is inactivating the sodium current on a slow timescale of about a second. Since slow inactivation of the sodium current is not a separate ionic current, as are the M-type, AHP-type, and sodium-activated potassium currents, but rather acts directly on a spike-generating current, this mechanism potentially behaves like the leaky integrate-and-fire model with a dynamic threshold. Note, however, that, formally, the slow inactivation can be separated from the fast activation and inactivation variables and thus should also resemble adaptation currents (Benda and Herz 2003). Figure 5 shows simulations of single-compartment conductance-based models with fast currents that explicitly generate action potentials and such adaptation currents. Adaptation induced by an AHP-type current, M-type current, or a sodium-activated potassium current clearly shifts the neuron's f–I curve to higher input currents (Fig. 5, A–E). No divisive effect on the f–I curve can be observed.

Also, both AHP-type and M-type adaptation currents in the Ermentrout (1998) model and the Prescott and Sejnowski (2008) model with AHP-type current demonstrate the linearizing effect of adaptation currents on the steady-state f–I curve (Fig. 5, A–C). The picture changes with adaptation currents that are activated at subthreshold membrane voltages, as for example the M-type current in the Prescott and Sejnowski (2008) model (Fig. 5D) or the sodium-activated potassium current in the Wang et al. (2003) model (Fig. 5E). In these cases, the activation of the adaptation current turns the neurons into type 2 excitable membranes with a discontinuity in their f–I curves (Ermentrout et al. 2001; Izhikevich 2000). Although adaptation currents still shift the adapted f–I curves to higher input intensities, the steady-state f–I curve is no longer linearized. Instead its threshold is moved to higher intensities.

Adaptation by slow inactivation of the sodium current, however, behaves in a completely different way (Fig. 5F). The prominent signature of this type of adaptation is neither a shift nor a scaling of the adapted f–I curves, but rather the rheobase
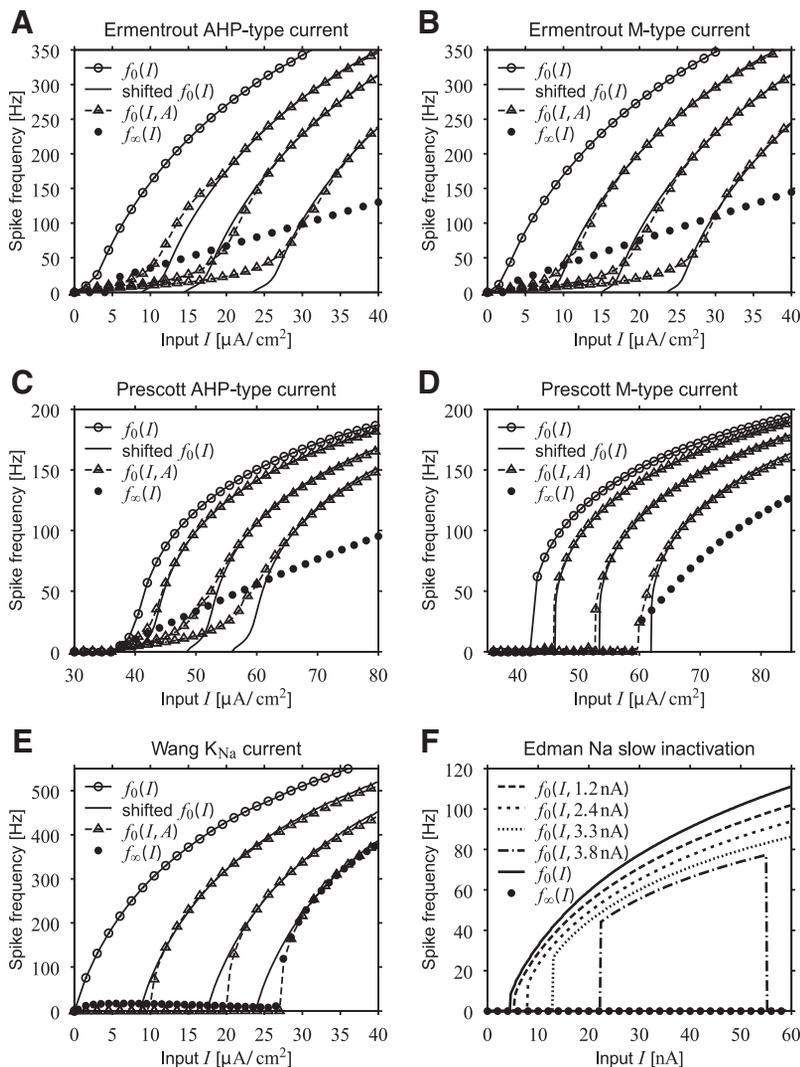

FIG. 5. Conductance-based models with adaptation currents show shifted f–I curves. Plotted are the onset f–I curve (open circles), adapted f–I curves (open triangles) in comparison with shifted onset f–I curves (solid lines), and the steady-state f–I curve (filled circles). A: adaptation caused by an afterhyperpolarization (AHP)-type current in the Traub–Miles model modified by Ermentrout (1998) shifts the neuron's onset f–I curve to higher input currents (I_0 = 10, 20, 30 μA/cm^2). B: an M-type current in the Ermentrout model (Ermentrout 1998) shifts the adapted f–I curves in a similar way (I_0 = 10, 20, 30 μA/cm^2). C: like the AHP-type current in the modified Morris–Lecar model by Prescott and Sejnowski (2008) (I_0 = 40, 50, 60 μA/cm^2). D: however, the M-type current in the Prescott model (Prescott and Sejnowski 2008) is already activated by subthreshold voltages and therefore induces type 2 excitability that is visible as the initial steps in the f–I curves. Still, at high spike frequencies, activation of the M-type current by spiking activity shifts the onset f–I curve to the right (I_0 = 40, 50, 60 μA/cm^2). E: a sodium-activated potassium current in a model of neurons in the primary visual cortex (Wang et al. 2003) also shifts the f–I curves (I_0 = 10, 20, 30 μA/cm^2). Here, the adaptation current is very strong and therefore brings the steady-state f–I curve close to zero. For input currents above $I \approx 27$ μA/cm^2 the adapted and the steady-state f–I curves match. F: adaptation evoked by slow inactivation of the sodium current behaves in a different way in that it mainly shifts the rheobase current to higher values and only weakly affects the f–I curves where they are nonzero (I_0 = 4, 6, 8, 10 nA). The example, a model of a lobster stretch receptor neuron (Edman et al. 1987), shows a mild divisive effect on the adapted f–I curves. The completely adapted neuron always ceases firing [$f_\infty(I) = 0 \ \forall \ I$]. See APPENDIX for model specifications.
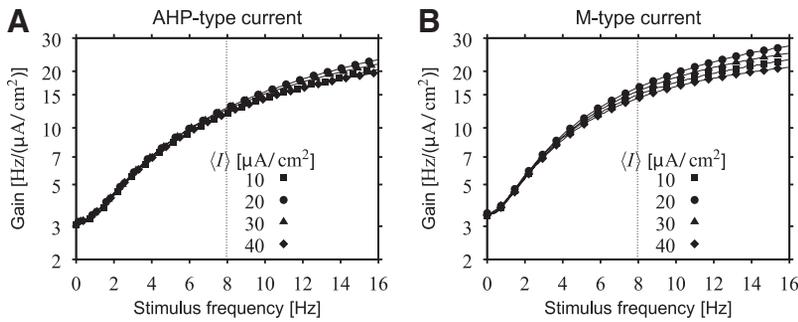
FIG. 6. High-pass filter properties of type 1 conductance-based models with adaptation currents. Shown is the gain computed for low-pass filtered (16 Hz) Gaussian white noise current with SD 2 μA/cm^2 and 4 different mean values $\langle I \rangle$, as indicated for the Ermentrout model (Ermentrout 1998) with an additional AHP-type current (*A*) or M-type current (*B*). In both cases the gain at low stimulus frequencies is independent of the mean intensity of the stimulus because the steady-state *f–I* curve is a linear function of *I* (see Fig. 5, *A* and *B*). Differences at high frequencies can be attributed to the nonlinear shape of the adapted *f–I* curves, resulting in different slopes at the intersections with the steady-state *f–I* curve with increasing mean of the stimulus and thus adaptation strength.

of the *f–I* curve is moved rightward, whereas the shape of the nonzero part of the *f–I* curve is only mildly affected. As a result, the continuous onset *f–I* curve with arbitrary low spike frequencies displays a growing discontinuity with stronger adaptation. This is a clear signature of a change from type 1 to type 2 excitability, which is not unexpected given that the slow sodium inactivation gating variable is already activated at subthreshold potentials and effectively decreases sodium conductance, which is a major determinant of spike generation (Ermentrout et al. 2001). Type 1 excitable membranes undergo a saddle-node bifurcation and are able to fire with arbitrary low rates, whereas type 2 membranes can fire only with nonzero frequencies as caused by the underlying Hopf bifurcation (Izhikevich 2000). In addition, with increasing sodium inactivation the current at which the cell goes into depolarization block moves to lower values [see $f_0(I, 3.8$ nA) curve in Fig. 5*F*].

The switch from type 1 to type 2 excitability that might be induced by activation of adaptation mechanisms (Fig. 5, *D–F*) is a phenomenon affecting the neuron close to its input threshold. Here (steady-state) spike frequencies are low and adaptation dynamics cannot be separated from the spike generator. In the remainder of this report we focus on the high firing rate regimes, where the two dynamics can be separated (spike frequency >1 over the adaptation time constant, i.e., in many cases ≳10 Hz). An investigation of the interaction between adaptation mechanisms and the excitability type will be published elsewhere (see also Ermentrout et al. 2001; Prescott and Sejnowski 2008).

As expected from the *f–I* curves the transfer functions resulting from AHP-type currents or M-type currents are high-pass and are largely independent of the mean current (Fig. 6). Deviations between the transfer functions can be attributed to possible nonlinear shapes of the onset and steady-state *f–I* curves.

Similar to our results for both the LIFAC and LIFDT (Fig. 4), AHP-type and M-type adaptation currents induce negative ISI correlations in the presence of additive white current noise (Fig. 7). However, strong anticorrelations extend over a larger range of spike frequencies and the minimum occurs at a frequency greater than the reciprocal of the adaptation time

constant (12.5 Hz for the AHP-type adaptation; 10 Hz for the M-type adaptation).

These simulations suggest that adaptation currents in conductance-based models with type 1 excitability could also be modeled as an adaptation current in the leaky integrate-and-fire model. In case an adaptation current switches a neuron to type 2 excitability, neither an adaptation current nor a dynamic threshold in an integrate-and-fire neuron can reproduce the properties of such conductance-based models at low spike frequencies. Note that regular-spiking pyramidal cells show both type 1 properties as well as spike-frequency adaptation and thus can be modeled with integrate-and-fire models with adaptation current (Jolivet et al. 2008; Rauch et al. 2003), whereas fast-spiking interneurons display type 2 *f–I* curves and much less adaptation (Tateno et al. 2004). In the following we investigate the effects of adaptation current and dynamic threshold in other types of integrate-and-fire neurons.

Perfect integrate-and-fire neuron

The perfect integrate-and-fire neuron (PIF) is the simplest of the family of integrate-and-fire models. At the same time it is the canonical model for limit cycle oscillations, i.e., all spiking-neuron models converge to the PIF at sufficiently high firing rates. This is exactly the regime we are focusing on in the following, i.e., on superthreshold spiking, where the ISIs are much shorter than the adaptation time constant.

The PIF integrates the input current independently of the membrane voltage

$$\tau_V \frac{dV}{dt} = RI \qquad (10)$$

As for the LIF, a spike is emitted and *V* is reset to V_r whenever *V* crosses the threshold V_{th}.

In the following we calculate the adapted *f–I* curves for the PIF with adaptation current (PIFAC) and with dynamic threshold (PIFDT) directly from the time courses of the membrane
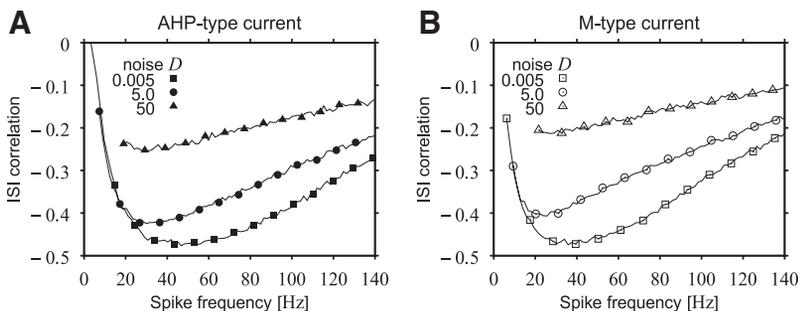

FIG. 7. Both the AHP-type current (*A*) and the M-type current (*B*) in the Ermentrout model (Ermentrout 1998) result in similar negative ISI correlations as a function of spike frequency and noise strength *D* of the additive Gaussian white noise given in μA · cm^{-2} · Hz^{-1}. The noise strength was chosen to result in CVs comparable to those in Fig. 4*D*. The negative correlations are strongest for weak noise strengths and peak at spike frequencies between 20 and 50 Hz. At higher as well as lower spike frequencies the correlations vanish.

potential and the adaptation variable, to make more general statements about the subtractive and divisive aspects of the different kinds of adaptation mechanisms.

Adapted f–I curve of the PIF with adaptation current. The differential equations for the membrane voltage V and the adaptation current A of the PIF with adaptation current (PIFAC) are the same as those for the LIFAC (*Eqs. 6 and 7*), except for the missing leak term $-V$.

Let us assume that there was a spike at time $t = 0$. Then the membrane potential is at $V(0) = V_r$ and the adaptation variable has some value $A(0) = A > 0$. As long as there is no further spike, according to the dynamics (*Eq. 7*) the adaptation current $A(t)$ decays back to zero with time constant τ_A

$$A(t) = Ae^{-t/\tau_A} \qquad (11)$$

Then, for $I = const$ the solution of the voltage dynamics is

$$V(t) = \frac{R}{\tau_V}\Big[It + A\tau_A(e^{-t/\tau_A} - 1)\Big] + V_r \qquad (12)$$

The next spike is emitted at $t = T$ when $V(t)$ crosses the threshold V_{th}. For ISIs T that are small compared with the adaptation time constant τ_A, $\exp(-T/\tau_A)$ can be approximated by $1 - T/\tau_A$. We then get for the adapted f–I curve

$$f_0(I, A) = \frac{1}{T} = \frac{R(I - A)}{\tau_V(V_{th} - V_r)} \qquad (13)$$

The current state of adaptation A is simply subtracted from the input and therefore the adaptation current shifts the f–I curve of

the PIFAC to the right without changing its shape (Fig. 8*A*). Consequently, the transfer function of the PIFAC is a high-pass filter that is independent of the mean current stimulus (Fig. 8*C*).

Adapted f–I curve of the PIF with dynamic threshold. Here, the solutions for the membrane potential (*Eq. 8* without leak term $-V$) and the dynamic threshold $A(t)$ (*Eq. 9*) are independent of each other

$$V(t) = \frac{R}{\tau_V} It + V_r \qquad (14)$$

$$A(t) = (A - V_{th})e^{-t/\tau_A} + V_{th} \qquad (15)$$

At the first passage time $t = T$ the voltage crosses the threshold and thus $V(T) = A(T)$. We must again approximate $\exp(-T/\tau_A)$ by $1 - T/\tau_A$ and end up with the following expression for the adapted f–I curve

$$f_0(I, A) = \frac{1}{T} = \frac{RI}{\tau_V(A - V_r)} + \frac{1}{\tau_A}\left(1 - \frac{V_{th} - V_r}{A - V_r}\right) \quad (16)$$

In the first term the current level of adaptation A (i.e., the current state of the voltage threshold) has a divisive effect on the resulting adapted f–I curve. The second term is always positive and it approximates $1/\tau_A$ for large A. The linear approximation of the dynamics of the adapting threshold, however, underestimates the adaptation strength at the threshold crossing of the following spike. Therefore *Eq. 16* overestimates the spike frequency (Fig. 8*B*, dotted line).

Because of this divisive effect of the current state of adaptation on the f–I curve, the transfer function strongly depends
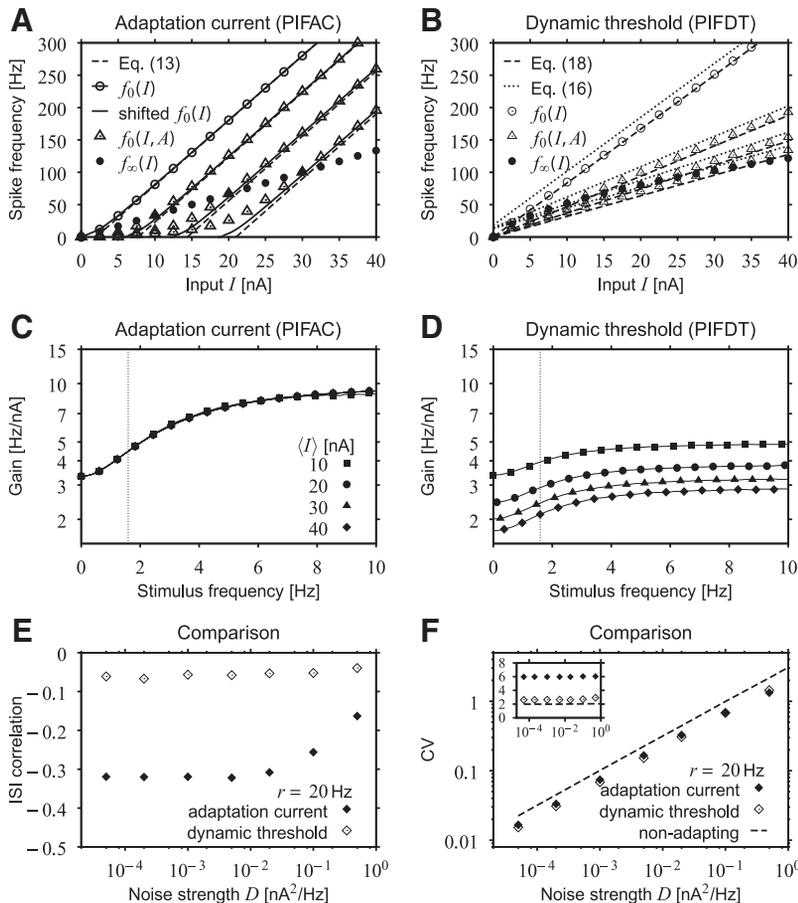

FIG. 8. Properties of the adapting perfect integrate-and-fire (PIF) models. *A*: the onset f–I curve (open circles) and the adapted f–I curves (open triangles) of the PIFAC for different levels of the adaptation current ($A = 7.7, 14, 21$ nA). The solid lines are the onset f–I curve shifted on top of the adapted f–I curves so that they intersect at a spike frequency of 200 Hz. The dashed lines are the predictions from the direct calculation (*Eq. 13*). The steady-state f–I curve is denoted by the filled circles. *B*: onset and adapted f–I curves of the PIFDT for different threshold values ($A = 21, 27, 31$ mV). The dashed lines are the predictions from the direct calculation (*Eq. 16*) and the averaging theory (*Eq. 18*). *C*: the gain functions of the PIFAC computed for low-pass filtered (16 Hz) Gaussian white noise current stimuli with SD 2 nA are independent of their mean $\langle I \rangle$, since the slope of the f–I curves is independent of the input current. The vertical dotted line here and in the next panel mark the frequency $(2\pi\tau_A)^{-1}$. The cutoff frequency of the high-pass filter caused by the adaptation current, however, is higher by a factor given by the relative slopes of the onset and the steady-state f–I curves (here ~ 3; Benda and Herz 2003). *D*: in contrast, the gain of the PIFDT is decreased for higher mean values of the stimulus, since the slopes of both the onset and the steady-state f–I curves are reduced by the dynamic threshold. *E*: the ISI correlations as a function of the noise strength D of the PIFDT are close to zero and much smaller than those of the PIFAC. The input current was adjusted to result in a firing rate of 20 Hz (see *inset* in *F*). *F*: the corresponding CVs, on the other hand, are almost identical and only slightly smaller than the CVs of the PIF without adaptation mechanism. The parameter values of the 2 PIF models were $\tau_V = 10$ ms, $V_{th} = 10$ mV, $V_r = 0$ mV, $R = 1$ MΩ, $\tau_A = 100$ ms, and $\Delta A = 2$ nA (PIFAC) or $\Delta A = 2$ mV (PIFDT).

on the mean of the current stimulus (Fig. 8*D*). The higher the input current, the lower the gain and the less pronounced the high-pass filter.

Interspike-interval correlations. Whereas for the LIF the negative correlations between successive ISIs were similar for both LIFAC and LIFDT, the PIFDT generates much weaker ISI correlations than the PIFAC (Fig. 8*E*). For the PIFDT the slope of even only weakly adapted *f–I* curves is similar to the slope of the steady-state *f–I* curve at a given mean stimulus intensity, showing that the adapting threshold has only a weak influence on the length of ISIs. This is in accordance with the weak high-pass filter component of the corresponding transfer function mentioned earlier. Therefore additive noise can generate only weak negative ISI correlations in the PIFDT because the effect of this noise on the adaptation dynamics is much smaller in the PIFDT than that in the PIFAC. Note, however, that the variability of the ISIs measured as the CV is almost identical in both models (Fig. 8*F*).

In contrast to the PIFDT, where the adapted *f–I* curves are perfectly scaled down and originate all at rheobase, the divisiveness of adaptation in the LIFDT acts on the current axis (see *Eq. 20* in the following text), resulting in stronger gain differences between adapted and steady-state *f–I* curves (Fig. 2*B*). Thus adaptation in the LIFDT still has a significant effect on ISIs and thus generates negative ISI correlations similar to the LIFAC.

Averaging theory

An alternative way for calculating the adapted *f–I* curves is to separate the fast dynamics of the membrane voltage from the slower dynamics of the adaptation current or the dynamic threshold. Then one can average over the slower adaptation dynamics and solve the voltage dynamics for the averaged and fixed adaptation variable (Benda and Herz 2003; Ermentrout 1998; Fohlmeister 1979; Wang 1998). This approach assumes again that the ISIs are short compared with the adaptation time constant.

For the models with adaptation current this is quite simple. If we know the *f–I* curve of the model without adaptation current, that is the onset *f–I* curve $f_0(I)$, then the adapted *f–I* curve simply reads $f(I, A) = f_0(I - A)$, since the adaptation current A is directly subtracted from the input I in the voltage dynamics. For the LIFAC this was derived by Fohlmeister (1979). Thus adaptation currents shift the neurons to higher input currents. This is a very general result for any kind of neuron model, as was shown by Benda and Herz (2003).

In the case of a dynamic threshold we need to know how the *f–I* curve of the model depends on the voltage threshold. For example, the *f–I* curve of the perfect integrate-and-fire neuron (*Eq. 10*) reads

$$f_{\text{PIF}}(I) = \frac{RI}{\tau_V(V_{th} - V_r)} \tag{17}$$

Thus with a dynamic threshold $V_{th}:= A$ and $V_r = 0$ we get for the adapted *f–I* curves of the PIFDT

$$f_{\text{PIF}}(I, A) = \frac{RI}{\tau_V A} \tag{18}$$

(dashed lines in Fig. 8*B*), which for high firing rates is indeed a good approximation of the adapted *f–I* curves. In *Eq. 18* the

dynamic threshold has a purely divisive effect on the *f–I* curve. Note also that *Eq. 18* is the first term of the direct solution (*Eq. 16*) we derived earlier.

The *f–I* curve of the LIF reads

$$f_{\text{LIF}}(I) = -\left[\tau_V \ln\left(\frac{RI - V_{th}}{RI - V_r} \right) \right]^{-1} \tag{19}$$

Again, for the LIFDT with $V_{th}:= A$ and $V_r = 0$ we get for the adapted *f–I* curve

$$f_{\text{LIF}}(I, A) = -\left[\tau_V \ln\left(1 - \frac{A}{RI} \right) \right]^{-1} \tag{20}$$

The dynamic threshold acts divisively on the input current I and thus stretches the *f–I* curve along the current axis (dashed lines in Fig. 2*B*).

Quadratic integrate-and-fire neuron

The quadratic integrate-and-fire neuron (QIF; Ermentrout 1996; Ermentrout and Kopell 1986; Fourcaud-Trocmé et al. 2003; Latham et al. 2000; Lindner et al. 2003) is the canonical model for a type 1 neuron, where periodic firing occurs through a saddle-node bifurcation (Ermentrout 1996; Rinzel and Ermentrout 1998). The dynamics of the membrane voltage obeys

$$\tau_V \frac{dV}{dt} = \frac{V^2}{2\Delta_T} + RI \tag{21}$$

where Δ_T is the spike slope factor (Fourcaud-Trocmé et al. 2003). Calculating the *f–I* curve of the QIF for arbitrary spiking threshold and reset yields

$$f_{\text{QIF}}(I) = \left(\frac{1}{\tau_V \sqrt{2\Delta_T}} \right) \times \left(\frac{\sqrt{RI}}{\arctan \frac{V_{th}}{\sqrt{2\Delta_T RI}} - \arctan \frac{V_r}{\sqrt{2\Delta_T RI}}} \right) \tag{22}$$

As expected, the QIF with an adaptation current (QIFAC; $I \rightarrow I - A$) shifts adapted *f–I* curves to higher input currents and linearizes the steady-state *f–I* curve (Fig. 9*A*).

For $V_{th} = \infty$ and $V_r = -\infty$, the usual values for the canonical form, the *f–I* curve of the QIF is a square-root function of the input

$$\lim_{\substack{V_{th} \rightarrow \infty \\ V_r \rightarrow -\infty}} f_{\text{QIF}}(I) = \sqrt{\frac{2}{\Delta_T}} \frac{\sqrt{RI}}{\pi \tau_V} \tag{23}$$

In this case, a dynamic threshold would not be able to generate any spike-frequency adaptation, since it does not matter whether the infinite threshold is further increased by each spike. Thus only for finite values of the threshold is the QIF with dynamic threshold (QIFDT) able to produce adapting responses. To get notable effects, the threshold must be quite low. The temporal derivative of the membrane potential quickly gets very large due to the quadratic term, so that changes in the threshold translate into tiny changes of the ISI.
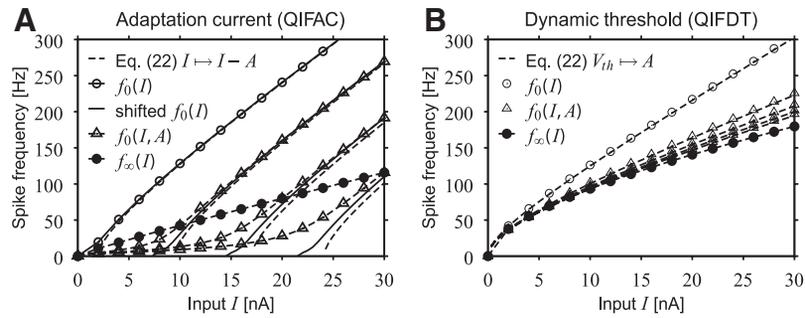
FIG. 9. A dynamic threshold has a small divisive effect in quadratic integrate-and-fire (QIF) models. *A*: the onset (open circles) and adapted *f*–*I* curves (open triangles) of the QIFAC for different levels of the adaptation current (*A* = 9.5, 17, 24 nA). The solid lines are the onset *f*–*I* curve shifted on top of the other *f*–*I* curves so that they intersect at a spike frequency of 200 Hz. The dashed lines are the predictions from the averaging theory using *Eq. 22* and replacing *I* by *I* − *A*. The steady-state *f*–*I* curve is denoted by the filled circles. *B*: onset *f*–*I* curves of the QIFDT for different threshold values (*A* = 11, 14, 17 mV). The dashed lines are the predictions from the averaging theory based on *Eq. 22* and replacing V_{th} by the dynamic threshold *A* (*Eq. 9*). The parameter values were $\tau_V = 10$ ms, $V_{th} = 2$ mV, $V_r = -8$ mV, $\Delta_T = 1$ mV, $R = 1$ MΩ, $\tau_A = 100$ ms, and $\Delta A = 2$ nA (QIFAC) or $\Delta A = 2$ mV (QIFDT).

For finite threshold and reset values and high-input values the *f*–*I* curve becomes linear and converges to the one of the PIF

$$\lim_{I \to \infty} f_{\text{QIF}}(I) = \frac{1}{\tau_V} \frac{RI}{V_{th} - V_r} \qquad (24)$$

Thus also for the QIFDT the dynamic threshold $V_{th} \to A(t)$ has a divisive effect on the adapted *f*–*I* curves (Fig. 9*B*). At high-input currents, the dynamic threshold hardly generates spike-frequency adaptation because the fixed threshold increments ΔA are increasingly less effective in altering the spike frequency.

Since the dynamic threshold has such a small influence on the adaptation behavior of the QIFDT it is not surprising that the QIFDT hardly generates any negative ISI correlations when driven with white noise stimuli. The QIF with adaptation current (QIFAC), on the other hand, shows negative ISI correlations very similar to those of the LIFAC (data not shown).

Exponential integrate-and-fire neuron

The exponential integrate-and-fire neuron is a modification of the QIF with a linear subthreshold dynamics (Fourcaud-Trocmé et al. 2003). The exponential term in the voltage dynamics

$$\tau_V \frac{dV}{dt} = -V + \Delta_T e^{(V - V_T)/\Delta_T} + RI \qquad (25)$$

simply mimics the spike-generating currents in conductance-based spiking models. V_T plays the role of the voltage threshold for spiking and the spike slope factor Δ_T determines the sharpness of the firing threshold. Together with the leak term a minimum is formed that resembles the quadratic form of the QIF. Thus the EIF also models type 1 excitability. As usual, *Eq. 25* is integrated until *V* crosses V_{th}, which usually equals ∞. Then a spike is emitted and integration is restarted at $V = V_r$, which is assumed to reflect a realistic reset potential.

With an adaptation current the EIFAC shows shifted *f*–*I* curves, as expected (Fig. 10*A*). A dynamic threshold $V_{th} \to A$ is able to produce some spike-frequency adaptation for only very low values of V_{th} (Fig. 10*C*), as was the case for the QIFDT. However, the effective voltage threshold for firing is

given by the threshold parameter V_T and not by V_{th}. Making this threshold adaptive we get

$$\tau_V \frac{dV}{dt} = -V + \Delta_T e^{(V - A)/\Delta_T} + RI \qquad (26)$$

$$\tau_A \frac{dA}{dt} = -A + V_T \qquad (27)$$

the EIF with adaptive threshold (EIFAT). Equivalent to the LIFDT, the EIFAT again generates adapted *f*–*I* curves that get less steep with increasing adaptation strength (Fig. 10*E*). This divisive effect is not surprising, since in the limit for very sharp spike initiation (i.e., $\Delta_T \to 0$), the EIFAT resembles the LIFDT.

Equivalently, for the QIF in the superthreshold regime the effective voltage threshold for firing is at the minimum of the quadratic function. This threshold can be made adaptive in the same way as for the EIFAT (*Eqs. 26* and *27*). For the standard threshold and reset voltages at +∞ and −∞, respectively, such a QIFAT obviously does not show any adaptation. Only for values of V_r close to the threshold voltage V_T does the adaptive threshold have a divisive effect on the onset *f*–*I* curves, very similar to the dynamic threshold shown in Fig. 9*B* (not shown).

With respect to the ISI correlations the EIF models behave similarly to the QIF models. An adaptation current clearly generates negative ISI correlations (Fig. 10*B*), as in the other integrate-and-fire models with adaptation currents. Since a dynamic threshold is hardly able to produce spike-frequency adaptation in the EIFDT the ISI correlations are also close to zero for all input currents (Fig. 10*D*). The adapting threshold parameter of the EIFAT is again able to induce negative ISI correlations (Fig. 10*F*).

DISCUSSION

Although at first glance integrate-and-fire models augmented with either an adaptation current or a dynamic threshold reproduce spike-frequency adaptation equally well (Fig. 1), they significantly differ in their signal processing properties. Based on the concept of "adapted *f*–*I* curves," i.e., onset *f*–*I* curves measured for various but fixed levels of adaptation, we have demonstrated by simulations and analytics that an adaptation current shifts the adapted *f*–*I* curves to the right (Benda and Herz 2003), whereas a dynamic threshold has a divisive
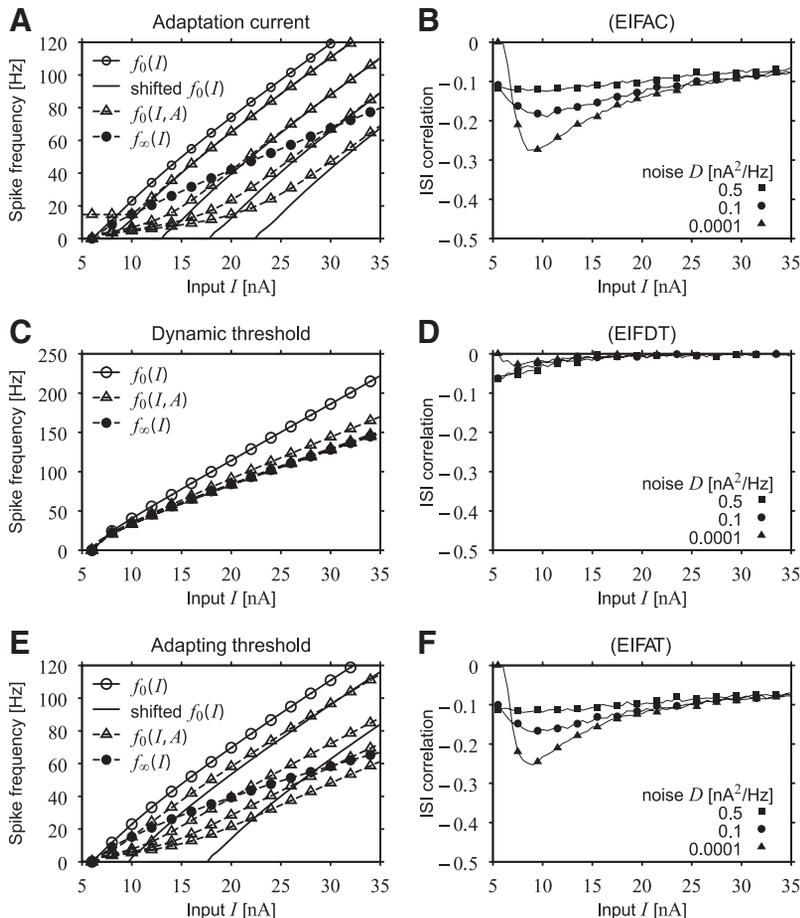
FIG. 10. Adaptation in 3 types of exponential integrate-and-fire (EIF) models. *A*, *C*, and *E*: the onset (open circles), adapted (open triangles), and steady-state (filled circle) *f–I* curves. The solid lines are the onset *f–I* curve shifted on top of the adapted *f–I* curves so that they intersect at a spike frequency of 100 Hz. *B*, *D*, and *F*: ISI correlations of the EIFs driven by constant currents with additive white noise of strength *D* as indicated. *A* and *B*: the EIF with adaptation current $I \rightarrow I - A$ for different levels of the adaptation current ($A = 4.0, 9.4, 14, 19$ nA) shifts the adapted *f–I* curves to the right and generates negative ISI correlations. *C* and *D*: the EIF with dynamic threshold $V_{th} \rightarrow A$ for different threshold values ($A = 12, 20, 30, 38$ mV) barely generates spike-frequency adaptation as well as ISI correlations. *E* and *F*: the EIF with adapting threshold parameter $V_T \rightarrow A$ for different threshold values ($A = 14, 19, 23, 26$ mV) has a divisive effect on the adapted *f–I* curves, but still shows negative ISI correlations. The parameter values were $\tau_V = 10$ ms, $V_{th} = 200$ mV (EIFAC, EIFAT) or $V_{th} = 12$ mV (EIFDT), $V_r = 0$ mV, $\Delta_T = 4$ mV, $V_T = 10$ mV, $R = 1$ MΩ, $\tau_A = 100$ ms, and $\Delta A = 2$ nA (EIFAC) or $\Delta A = 2$ mV (EIFDT, EIFAT).

effect on these onset *f–I* curves. This is one fingerprint of the primarily linear characteristics of an adaptation current and the nonlinear characteristics of a dynamic threshold. A further aspect is the independence of the high-pass filter component of the neuron's transfer function from the mean of the stimulus, and thus adaptation level, in the models with adaptation current, whereas with a dynamic threshold the properties of the high-pass filter strongly depend on stimulus mean.

The high-pass filter property associated with both the spike-frequency adaptation and the subtractive effect on adapted *f–I* curves has been experimentally shown to play an important role in enhancing the response to fast components of communication signals in weakly electric fish (Benda et al. 2005) or to generate intensity-invariant responses in the auditory system of crickets (Benda and Hennig 2008). Here we have shown by simulations of a range of conductance-based models that adaptation currents indeed have a subtractive effect on adapted *f–I* curves and generate a high-pass filter that is independent of the mean intensity of a stimulus. These simulations therefore strongly suggest that spike-frequency adaptation caused by adaptation currents should be modeled as adaptation currents in integrate-and-fire neurons and not as a dynamic threshold.

Note that we have focused here on the dynamic effects of the adaptation variable (current or threshold) on the transient onset response to current steps while keeping all parameter values constant. These onset or adapted *f–I* curves determine the signal-transmission properties of high-frequency stimulus components that are considerably faster than the adaptation time constant. On the other hand, numerous studies have

investigated how changes in model parameters, like the adaptation strength (here ΔA, or more generally the strength of some inhibitory feedback) or noise intensity, influence the shape of the steady-state *f–I* curve. In particular, with or without noise, the adaptation strength acts divisively on this steady-state *f–I* curve in both adaptation current and dynamic threshold models (see Sutherland et al. 2009 and references therein). Adaptation currents tend to linearize the steady-state *f–I* curve compared with the onset *f–I* curve or the steady-state *f–I* curve of the corresponding neuron without adaptation (zero adaptation strength) (Benda and Herz 2003; Ermentrout 1998). In contrast, herein we report that the steady-state *f–I* curves of the models with dynamic threshold are more concave (rightward curved) than the *f–I* curve of the model without adaptation.

Negative correlations between successive ISIs have been observed in many sensory as well as cortical neurons (for a review, see Farkhooi et al. 2009). In electroreceptor neurons of weakly electric fish they have been studied in great detail (Ratnam and Nelson 2000), mainly by means of a leaky integrate-and-fire model with dynamic threshold (Chacron et al. 2000). The negative ISI correlations improve information transmission (Chacron et al. 2001) by reducing low-frequency noise (Chacron et al. 2005; Lindner et al. 2005). In all these studies, however, the underlying adaptation mechanisms have not been elucidated. Later, Benda et al. (2005) measured a subtractive effect of adaptation on *f–I* curves of the electroreceptor neurons that, in the light of our results, suggests an adaptation current, not a dynamic threshold, in these neurons.

Nevertheless, both a dynamic threshold and an adaptation current are able to induce negative ISI correlations in the leaky integrate-and-fire neuron (Fig. 4; Liu and Wang 2001). Therefore the conclusions on the effect of negative ISI correlations on information transmission should be independent of the specific adaptation mechanism. However, here we show that in the perfect, the quadratic, and the exponential integrate-and-fire neuron negative ISI correlations are much weaker with a dynamic threshold than an adaptation current. This demonstrates that an adaptation current generates ISI anticorrelations more robustly, i.e., independently of the specific dynamics of the spike generator, than a dynamic threshold. Our simulations suggest that, for a given input current, the maximum strength of the ISI anticorrelations reflects the effectiveness of the adaptation mechanism and that this can be experimentally assessed by the relative slopes of the corresponding adapted f–I curve and the steady-state f–I curve. The more similar these two slopes are, the less effective is the adaptation mechanism and the less the neuron adapts and is able to generate ISI correlations.

In a previous comparison, only quantitative differences were reported between LIFAC and LIFDT (Liu and Wang 2001). Lindner and Longtin (2003) indeed derived a mapping of the leaky integrate-and-fire neuron with dynamic threshold to that with an adaptation current, further supporting the strong similarity between these two models. However, the mapped dynamic-threshold model includes scaling factors for the input current as well as the adaptation current that depend on the mean adaptation level. These scaling factors introduce the divisiveness of the dynamic threshold that we report herein. Thus as long as the mean adaptation level is approximately constant, both models behave similarly. However, as soon as strong low-frequency stimuli significantly drive the adaptation dynamics, the mean adaptation level changes and the two models show qualitatively distinct properties.

Here we have focused on the effects of adaptation mechanisms on the superthreshold firing regime, where the ISIs are shorter than the adaptation time constant. This allowed us to average over the slow adaptation dynamics (Benda and Herz 2003; Ermentrout 1998; Fohlmeister 1979; Wang 1998) and to derive expressions for the adapted f–I curves. However, as our simulations of conductance-based models show, adaptation currents that are already activated by subthreshold voltages (Fig. 5, *D–F*) often turn a type 1 neuron with a continuous f–I curve into a type 2 neuron with a discontinuity in its f–I curve (Ermentrout et al. 2001; Prescott and Sejnowski 2008). Such subthreshold-activated adaptation currents have been incorporated in integrate-and-fire models by adding a linear dependence on the membrane potential to the adaptation current's activation function (Brette and Gerstner 2005; Izhikevich 2003), as was already done for modeling accommodation (Hill 1936). These two-dimensional models can describe a wide variety of firing patterns, including spike-frequency adaptation, bursting, subthreshold, and oscillations, for example (Izhikevich 2004; Naud et al. 2008), and can reproduce the dynamics of a detailed conductance-based model (Brette and Gerstner 2005) as well as experimental data (Jolivet et al. 2008).

Voltage traces of intracellularly recorded adapting neurons sometimes show an increasing firing threshold during the course of spike-frequency adaptation in accordance with the models with dynamic threshold (see, e.g., Mason and Larkman 1990; Figs. 4, *A* and *B* and 7, *A* and *B* or Chacron et al. 2007; Fig. 2). However, intrinsically generated adaptation is thought to be primarily based on adaptation currents, like the M-type (Brown and Adams 1980) or AHP-type currents (Madison and Nicoll 1984). These slow ionic currents modulate the dynamics of fast spike-generating processes (Benda and Herz 2003; Ermentrout 1998; Wang 1998) and therefore may also induce the observed changes in firing threshold. In agreement with our results this suggests that a dynamic firing threshold is not causing spike-frequency adaptation, but rather is a secondary effect resulting from the action of an adaptation current. Therefore we strongly suggest modeling spike-frequency adaptation in integrate-and-fire models as a (simplified) adaptation current that is causing the spike-frequency adaptation and not as a dynamic threshold.

In this sense, to our knowledge, no biophysical mechanism is known that primarily modulates a neuron's firing threshold on timescales larger than tens of milliseconds as in the integrate-and-fire models with dynamic threshold discussed here. This does not exclude that adaptation currents, like M-type or AHP-type currents, or sodium-activated potassium currents, might affect the neuron's firing threshold. Also, our simulations demonstrate that slow inactivation of sodium currents, as the most promising known mechanism for resembling the properties of integrate-and-fire neurons with dynamic threshold, increases the rheobase and produces abrupt jumps in spike frequency at rheobase, but only slightly changes the slope of the f–I curve (Fig. 5F). This behavior differs from the divisive effect of a pure dynamic threshold on the neuron's adapted f–I curves.

Chacron et al. (2007) suggested a hypothetical dynamic half-activation and half-inactivation voltage of the sodium current and demonstrated that this mechanism generates threshold variability and negative ISI correlations. In this model this threshold dynamics indeed has a divisive effect on adapted f–I curves (not shown), in accordance with our results. Azouz and Gray (2000) previously reported threshold fluctuations in cortical cells, although it is not known whether they are produced by the proposed biophysical mechanism reported by Chacron and colleagues; it would therefore be of interest to investigate the effect of preadaptation on f–I curves in these neurons.

Our results emphasize that there is a functional difference between potential mechanisms that directly operate on the neuron's firing threshold and mechanisms, like ionic currents, that might only secondarily affect the threshold. To distinguish these two cases in a neuron showing threshold fluctuations, we suggest measuring adapted f–I curves. If the threshold variability is only a byproduct of an adaptation current then the adapted f–I curves should be shifted along the current axis. If, on the other hand, a yet unknown mechanism directly modulates the firing threshold then it should reveal itself by a divisive effect on the f–I curves.

APPENDIX

Specifications of conductance-based models

Here we specify the equations and parameters of the conductance-based models used for the simulations shown earlier in Figs. 5, 6, and 7. Implementations of the models in C++ can be obtained from the RELACS electrophysiological data-acquisition framework at www.relacs.net in the files spikingneuron.h and spikingneuron.cc

of the ephys plugin set (classes TraubErmentrout1998; MorrisLecarPrescott, WangIKNa, and Edman).

ERMENTROUT MODEL.   The Ermentrout model is a one-compartment version of the Traub–Miles model, as introduced by Ermentrout (1998). The membrane equation for the membrane potential V (measured in mV) reads

$$C \frac{dV}{dt} = -I_{Na} - I_K - I_L - I_{Ca} - I_M - I_{AHP} + I$$

with the voltage-gated sodium current $I_{Na} = \bar{g}_{Na} m^3 h(V - E_{Na})$, voltage-gated potassium current $I_K = \bar{g}_K n^4 (V - E_K)$, leak current $I_L = \bar{g}(V - E_L)$, voltage-gated calcium current $I_{Ca} = \bar{g}_{Ca}\{1 + \exp[-(V + 25)/5]\}^{-1}(V - E_{Ca})$, M-type current $I_M = \bar{g}_M w(V - E_K)$, and AHP-type current $I_{AHP} = \bar{g}_{AHP}[Ca](30 + [Ca])^{-1}(V - E_K)$. The kinetics of the gating variables $x \in m, h, n$ obeys

$$\frac{dx}{dt} = \alpha_x(1 - x) - \beta_x x$$

with $\alpha_m = 0.32(V + 54)/\{1 - \exp[-(V + 54)/4]\}$, $\beta_m = 0.28(V + 27)/\{\exp[(V + 27)/5] - 1\}$, $\alpha_h = 0.128 \exp[-(V + 50)/18]$, $\beta_h = 4/\{1 + \exp[-(V + 27)/5]\}$, $\alpha_n = 0.032(V + 52)/\{1 - \exp[-(V + 52)/5]\}$, $\beta_n = 0.5 \exp[-(V + 57)/40]$. The kinetics of w of the M-type current follows

$$\tau_w \frac{dw}{dt} = \frac{1}{1 + \exp[-(V + 20)/5]} - w$$

and that for the intracellular calcium concentration [Ca] (in mM) reads

$$\frac{d[Ca]}{dt} = -0.002 I_{Ca} - 0.0125[Ca]$$

Values of the conductances are $\bar{g}_{Na} = 100$ mS/cm^2, $\bar{g}_K = 80$ mS/cm^2, $\bar{g}_L = 0.1$ mS/cm^2, $\bar{g}_{Ca} = 1$ mS/cm^2, $\bar{g}_M = 16$ mS/cm^2, $\bar{g}_{AHP} = 30$ mS/cm^2; the reversal potentials are $E_{Na} = +50$ mV, $E_K = -100$ mV, $E_L = -67$ mV, $E_{Ca} = +120$ mV; the membrane capacitance is $C = 1$ μF/cm^2; and the time constant of the M-type current gating variable $\tau_w = 100$ ms.

For the model with AHP-type current (Figs. 5A, 6A, and 7A) we set $\bar{g}_M = 0$ and for the model with M-type current (Figs. 5B, 6B, and 7B), $\bar{g}_{AHP} = 0$.

PRESCOTT MODEL.   The Prescott model is the Morris–Lecar model extended by an adaptation current I_A (Prescott and Sejnowski 2008). The membrane equation for the membrane potential V (measured in mV) reads

$$C \frac{dV}{dt} = -I_{Ca} - I_K - I_L - I_A + I$$

with the calcium current $I_{Ca} = \bar{g}_{Ca}\{1 + \exp[-2(V + 1.2)/18]\}^{-1}(V - E_{Ca})$, potassium current $I_K = \bar{g}_K w(V - E_K)$, leak current $I_L = \bar{g}_L(V - E_L)$, and adaptation current $I_A = \bar{g}_A z(V - E_K)$. The kinetics of the gating variables w and z is given by

$$\frac{1}{0.15 \cosh(0.5V/10)} \frac{dw}{dt} = \frac{1}{1 + \exp(-2V/10)} - w$$

$$\tau_A \frac{dz}{dt} = \frac{1}{1 + \exp[-(V - V_A)/4]} - z$$

Values of the conductances are $\bar{g}_{Ca} = 20$ nS, $\bar{g}_K = 20$ nS, $\bar{g}_L = 2$ nS; the reversal potentials are $E_{Ca} = +50$ mV, $E_K = -100$ mV, $E_L = -70$ mV; the membrane capacitance is $C = 2$ pF; and the adaptation time constant $\tau_A = 100$ ms.

For the model with AHP-type current (Fig. 5C) $\bar{g}_A = 5$ nS and $V_A = 0$ mV. For the model with M-type current (Fig. 5D) $\bar{g}_A = 1.5$ nS and $V_A = -35$ mV.

WANG MODEL.   The Wang model includes a sodium-activated potassium current I_{KNa}, causing very slow spike-frequency adaptation (Wang et al. 2003; Fig. 5E). We removed the coupling to the dendritic compartment as well as the calcium-gated potassium current, to focus on the effects of the sodium-gated potassium current. The resulting single membrane equation for the somatic membrane potential V (measured in mV) reads

$$C \frac{dV}{dt} = -I_{Na} - I_K - I_L - I_{Ca} - I_{IKNa} + I$$

with the voltage-gated sodium current $I_{Na} = \bar{g}_{Na}\{1 + 4 \exp[-(V + 58)/12]\{\exp[-0.1(V + 33)] - 1\}/[-0.1(V + 33)]\}\rangle^{-3} h(V - E_{Na})$, voltage-gated potassium current $I_K = \bar{g}_K n^4 (V - E_K)$, leak current $I_L = \bar{g}_L(V - E_L)$, voltage-gated calcium current $I_{Ca} = \bar{g}_{Ca}\{1 + \exp[-(V + 20)/9]\}^{-2}(V - E_{Ca})$, and sodium-gated potassium current $I_{KNa} = \bar{g}_{KNa} 0.37/[1 + (38.7/[Na])^{3.5}](V - E_K)$. Kinetics of the two gating variables h and n, respectively, are given by

$$0.25 \frac{dh}{dt} = 0.07 \exp[-(V + 50)/10](1 - h)$$
$$- \frac{1}{\exp[-0.1(V + 20)] + 1} h$$

$$0.25 \frac{dn}{dt} = \frac{-0.01(V + 34)}{\exp[-0.1(V + 34)] - 1}(1 - n)$$
$$- 0.125 \exp[-(V + 44)/25]n$$

The kinetics for the intracellular calcium concentration [Ca] (in mM) follows

$$\frac{d[Ca]}{dt} = -0.002 I_{CaS} - [Ca]/240$$

and the kinetics of the sodium concentration [Na] is

$$\frac{d[Na]}{dt} = -0.0003 I_{Na} - 3 \cdot 0.0006 \left(\frac{[Na]^3}{[Na]^3 + 15^3} - \frac{8^3}{8^3 + 15^3} \right)$$

Values of the conductances are $\bar{g}_{Na} = 45$ mS/cm^2, $\bar{g}_K = 18$ mS/cm^2, $\bar{g}_L = 0.1$ mS/cm^2, $\bar{g}_{Ca} = 1$ mS/cm^2, $\bar{g}_{KNa} = 3$ mS/cm^2; the reversal potentials are $E_{Na} = +55$ mV, $E_K = -80$ mV, $E_L = -65$ mV, $E_{Ca} = +120$ mV; and the membrane capacitance is $C = 1$ μF/cm^2.

EDMAN MODEL.   The Edman model is a one-compartment model with slow inactivation of the sodium current (Edman et al. 1987; Fig. 5F). The membrane equation for the membrane potential V (measured in mV) reads

$$AC \frac{dV}{dt} = -I_{Na} - I_K - I_{LNa} - I_{LK} - I_{LCl} - I_P + 0.001I$$

with the voltage-gated sodium $I_{Na} = P_{Na} m^2 h l \phi_{Na}(V)$ (where l is the gating variable responsible for slow inactivation) and potassium current $I_K = P_K n^2 r \phi_K(V)$, the sodium $I_{LNa} = P_{LNa} \phi_{Na}(V)$, potassium $I_{LK} = P_{LK} \phi_K(V)$, and chloride leak current $I_{LCl} = P_{LCl} \phi_{Cl}(V)$, where

$$\phi_Y(V) = AV \frac{F^2}{RT} \frac{[Y]_o - [Y]_i \exp\left(-\frac{VF}{RT}\right)}{1 - \exp\left(-\frac{VF}{RT}\right)}$$

The sodium-pump current is $I_P = 10^6 A P_P F/\{3(1 + 7.7 \text{ mM}/[Na]_i)^3\}$ and the input current I is measured in nA. The kinetics of the gating variables $x \in m, h, l, n$, and r is given by

$$\tau_x \frac{dx}{dt} = x_\infty - x$$

with

$$x_\infty = v_x + \frac{1 - v_x}{1 + \exp\left[-\dfrac{z_x e}{kT}(V - V_x)\right]}$$

and

$$\tau_x = \bar{\tau}_x \frac{\left(\dfrac{1 - d_x}{d_x}\right)^{d_x} + \left(\dfrac{1 - d_x}{d_x}\right)^{d_x - 1}}{\exp\left[-d_x \dfrac{z_x e}{kT}(V - V_x)\right] + \exp\left[-(d_x - 1)\dfrac{z_x e}{kT}(V - V_x)\right]}$$

The parameter values are $d_m = 0.3$, $d_h = 0.5$, $d_l = 0.3$, $d_n = 0.3$, $d_r = 0.5$; $z_m = 3.1$, $z_h = -4.0$, $z_l = -3.5$, $z_n = 2.6$, $z_r = -4.0$; $v_m = 0.0$, $v_h = 0.0$, $v_l = 0.0$, $v_n = 0.03$, $v_r = 0.3$; $V_m = -13.0$ mV, $V_h = -35.0$ mV, $V_l = -53.0$ mV, $V_n = -18.0$ mV, $V_r = -61.0$ mV; $\bar{\tau}_m = 0.3$ ms, $\bar{\tau}_h = 5.0$ ms, $\bar{\tau}_l = 1{,}700.0$ ms, $\bar{\tau}_n = 6.0$ ms, $\bar{\tau}_r = 1{,}200.04$ ms; temperature $T = 291$ K; Faraday constant F $= 96{,}485$ C/mol; gas constant $R = 8{,}314.4$ mJ $\cdot$ K$^{-1} \cdot$ mol^{-1}; electron charge $e = 1.60217653 \times 10^{-22}$ kC; Boltzman constant $k = 1.3806505 \times 10^{-23}$ J/K.

The kinetics for the intracellular sodium concentration $[Na]_i$ (in mM) is as follows

$$1{,}000 F Vol \frac{d[Na]_i}{dt} = -I_{Na} - I_{LNa} - 3I_P$$

The extracellular concentrations are $[Na]_o = 325$ mM, $[K]_o = 5$ mM, and $[Cl]_o = 414$ mM. The intracellular concentration of chloride is $[Cl]_i = 46$ mM. The intracellular concentrations of sodium and potassium at rest are $[Na]_r = 10$ mM and $[K]_r = 160$ mM, respectively. The intracellular concentration of potassium is then given by $[K]_i = [K]_r - ([Na]_i - [Na]_r)$.

The permeabilities are $P_{Na} = 5.6 \times 10^{-4}$ cm/s, $P_K = 2.4 \times 10^{-4}$ cm/s, $P_{LNa} = 5.8 \times 10^{-8}$ cm/s, $P_{LK} = 1.8 \times 10^{-6}$ cm/s, $P_{LCl} = 1.1 \times 10^{-7}$ cm/s, $P_P = 3.0 \times 10^{-10}$ mol $\cdot$ cm$^{-2} \cdot$ s^{-1}, the membrane capacitance is $C = 7.8$ μF/cm^2, the cell surface $A = 0.001$ cm^2, and the cell volume $Vol = 1.25 \times 10^{-6}$ cm^3.

REFERENCES

Azouz R, Gray CM. Dynamic spike threshold reveals a mechanism for synaptic coincidence detection in cortical neurons *in vivo*. *Proc Natl Acad Sci USA* 97: 8110–8115, 2000.

Benda J, Hennig RM. Dynamics of intensity invariance in a primary auditory interneuron. *J Comput Neurosci* 24: 113–136, 2008.

Benda J, Herz AVM. A universal model for spike-frequency adaptation. *Neural Comput* 15: 2523–2564, 2003.

Benda J, Longtin A, Maler L. Spike-frequency adaptation separates transient communication signals from background oscillations. *J Neurosci* 25: 2312–2321, 2005.

Bibikov NG, Ivanitskíí GA. Simulation of spontaneous discharge and short-term adaptation in acoustic nerve fibers. *Biofizika* 30: 141–144, 1985.

Brette R, Gerstner W. Adaptive exponential integrate-and-fire model as an effective description of neuronal activity. *J Neurophysiol* 94: 3637–3642, 2005.

Brown DA, Adams PR. Muscarinic suppression of a novel voltage-sensitive K$^+$ current in a vertebrate neuron. *Nature* 183: 673–676, 1980.

Chacron MJ, Lindner B, Longtin A. Threshold fatigue and information transfer. *J Comput Neurosci* 23: 301–311, 2007.

Chacron MJ, Longtin A, Maler L. Negative interspike interval correlations increase the neuronal capacity for encoding time-dependent stimuli. *J Neurosci* 21: 5328–5343, 2001.

Chacron MJ, Longtin A, St-Hilaire M, Maler L. Suprathreshold stochastic firing dynamics with memory in P-type electroreceptors. *Phys Rev Lett* 85: 1576–1579, 2000.

Chacron MJ, Maler L, Bastian J. Electroreceptor neuron dynamics shape information transmission. *Nat Neurosci* 8: 673–678, 2005.

Edman Å, Gestrelius S, Grampp W. Analysis of gated membrane currents and mechanisms of firing control in the rapidly adapting lobster stretch receptor neurone. *J Physiol* 384: 649–669, 1987.

Ermentrout B. Type I membranes, phase resetting curves, and synchrony. *Neural Comput* 8: 979–1001, 1996.

Ermentrout B. Linearization of f–I curves by adaptation. *Neural Comput* 10: 1721–1729, 1998.

Ermentrout B, Pascal M, Gutkin B. The effects of spike frequency adaptation and negative feedback on the synchronization of neural oscillators. *Neural Comput* 13: 1285–1310, 2001.

Ermentrout GB, Kopell N. Parabolic bursting in an excitable system coupled with a slow oscillation. *SIAM J Appl Math* 46: 233–253, 1986.

Farkhooi F, Strube-Bloss MF, Nawrot MP. Serial correlation in neural spike trains: Experimental evidence, stochastic modeling, and single neuron variability. *Phys Rev E* 79: 021905, 2009.

Fleidervish IA, Friedman A, Gutnick MJ. Slow inactivation of Na$^+$ current and slow cumulative spike adaptation in mouse and guinea-pig neocortical neurones in slices. *J Physiol* 4931: 83–97, 1996.

Fohlmeister JF. A theoretical study of neural adaptation and transient responses due to inhibitory feedback. *Bull Math Biol* 41: 257–282, 1979.

Fourcaud-Trocmé N, Hansel D, van Vreeswijk C, Brunel N. How spike generation mechanisms determine the neuronal response to fluctuating inputs. *J Neurosci* 23: 11628–11640, 2003.

Geisler CD, Goldberg JM. A stochastic model of the repetitive activity of neurons. *Biophys J* 6: 53–69, 1966.

Gigante G, Giudice PD, Mattia M. Frequency-dependent response properties of adapting spiking neurons. *Math Biosci* 207: 336–351, 2007.

Hill AV. Excitation and accommodation in nerve. *Proc R Soc Lond B Biol Sci* 119: 305–355, 1936.

Holden AV. Models of the stochastic activity of neurons. In: *Lecture Notes in Biomathematics*. Berlin: Springer-Verlag, 1976, vol. 12.

Izhikevich EM. Neural excitability, spiking, and bursting. *Int J Bifurc Chaos* 10: 1171–1266, 2000.

Izhikevich EM. Simple model of spiking neurons. *IEEE Trans Neural Netw* 14: 1569–1572, 2003.

Izhikevich EM. Which model to use for cortical spiking neurons? *IEEE Trans Neural Netw* 15: 1063–1070, 2004.

Jolivet R, Kobayashi R, Rauch A, Naud R, Shinomoto S, Gerstner W. A benchmark test for a quantitative assessment of simple neuron models. *J Neurosci Methods* 169: 417–424, 2008.

Lapicque L. Quantitative investigations of electrical nerve excitation treated as polarization: Louis Lapicque 1907, translated from French by Brunel N, van Rossum MCW. *Biol Cybern* 97: 341–349, 2007.

Latham PE, Richmond BJ, Nelson PG, Nirenberg S. Intrinsic dynamics in neuronal networks. II. Experiment. *J Neurophysiol* 83: 808–827, 2000.

Lindner B, Chacron MJ, Longtin A. Integrate-and-fire neurons with threshold noise: a tractable model of how interspike interval correlations affect neuronal signal transmission. *Phys Rev E* 72: 021911, 2005.

Lindner B, Longtin A. Nonrenewal spike trains generated by stochastic neuron models. *Proc SPIE* 5114: 209–218, 2003.

Lindner B, Longtin A. Effect of an exponentially decaying threshold on the firing statistics of a stochastic integrate-and-fire neuron. *J Theor Biol* 232: 505–521, 2005.

Lindner B, Longtin A, Bulsara A. Analytic expressions for rate and CV of a type I neuron driven by white Gaussian noise. *Neural Comput* 15: 1760–1787, 2003.

Liu YH, Wang XJ. Spike-frequency adaptation of a generalized leaky integrate-and-fire model neuron. *J Comput Neurosci* 10: 25–45, 2001.

Madison DV, Nicoll RA. Control of the repetitive discharge of rat CA1 pyramidal neurones in vitro. *J Physiol* 354: 319–331, 1984.

Mason A, Larkman A. Correlations between morphology and electrophysiology of pyramidal neurons in slices of rat visual context. II. Electrophysiology. *J Neurosci* 10: 1415–1428, 1990.

Naud R, Marcille N, Clopath C, Gerstner W. Firing patterns in the adaptive exponential integrate-and-fire model. *Biol Cybern* 99: 335–347, 2008.

Peron S, Gabbiani F. Spike frequency adaptation mediates looming stimulus selectivity in a collision-detecting neuron. *Nat Neurosci* 12: 318–326, 2009.

Prescott SA, Sejnowski TJ. Spike-rate coding and spike-time coding are affected oppositely by different adaptation mechanisms. *J Neurosci* 28: 13649–13661, 2008.

Ratnam R, Nelson ME. Nonrenewal statistics of electrosensory afferent spike trains: implications for the detection of weak sensory signals. *J Neurosci* 20: 6672–6683, 2000.

Rauch A, Camera GL, Lüscher HR, Senn W, Fusi S. Neocortical pyramidal cells respond as integrate-and-fire neurons to in vivo-like input currents. *J Neurophysiol* 90: 1598–1612, 2003.

Rinzel J, Ermentrout B. Analysis of neural excitability and oscillations. In: *Methods in Neural Modeling*, edited by Koch C, Segev I. Cambridge, MA: MIT Press, 1998, p. 251–292.

Sah P. Ca^{2+}-activated K^+ currents in neurones: types, physiological roles and modulation. *Trends Neurosci* 19: 150–154, 1996.

Sobel EC, Tank DW. In vivo Ca^{2+} dynamics in a cricket auditory neuron: an example of chemical computation. *Science* 263: 823–826, 1994.

Stein RB. A theoretical analysis of neuronal variability. *Biophys J* 5: 173–194, 1965.

Sutherland C, Doiron B, Longtin A. Feedback-induced gain control in stochastic spiking networks. *Biol Cybern* 100: 475–489, 2009.

Tateno T, Harsch A, Robinson HP. Threshold firing frequency–current relationships of neurons in rat somatosensory cortex: type 1 and type 2 dynamics. *J Neurophysiol* 92: 2283–2294, 2004.

Treves A. Mean-field analysis of neuronal spike dynamics. *Network Comput Neural Syst* 4: 259–284, 1993.

Tuckwell HC. Recurrent inhibition and afterhyperpolarization: effects on neuronal discharge. *Biol Cybern* 30: 115–123, 1978.

Wang XJ. Calcium coding and adaptive temporal computation in cortical pyramidal neurons. *J Neurophysiol* 79: 1549–1566, 1998.

Wang XJ, Liu Y, Sanchez-Vives M, McCormick D. Adaptation and temporal decorrelation by single neurons in the primary visual cortex. *J Neurophysiol* 89: 3279–3293, 2003.

Wilbur WJ, Rinzel J. A theoretical basis for large coefficient of variation and bimodality in neuronal interspike interval distributions. *J Theor Biol* 105: 345–368, 1983.